crystals

MDPI

Article

Theoretical Examination of the Radiation Protecting Properties of $CaTiO_3$ Material Sintered at Different Temperatures

Essia Hannachi [1], M. I. Sayyed [2,3,*], Suhairul Hashim [3], Karem Mahmoud [4] and Yassine Slimani [5]

[1] Department of Nuclear Medicine Research, Institute for Research and Medical Consultations (IRMC), Imam Abdulrahman bin Faisal University, P.O. Box 1982, Dammam 31441, Saudi Arabia
[2] Department of Physics, Faculty of Science, Isra University, Amman 11622, Jordan
[3] Physics Department, Faculty of Science, Universiti Teknologi Malaysia, Skudai 81310, Malaysia
[4] Department of Nuclear Power Plants and Renewable Energy, Ural Energy Institute, Ural Federal University, 19 Mira Street, 620002 Yekaterinburg, Russia
[5] Department of Biophysics, Institute for Research and Medical Consultations (IRMC), Imam Abdulrahman bin Faisal University, P.O. Box 1982, Dammam 31441, Saudi Arabia
* Correspondence: dr.mabualssayed@gmail.com

Abstract: This research is devoted to studying the radiation-protecting characteristics of calcium titanate ($CaTiO_{3)}$ perovskite-based ceramic material. The ceramics were made by the solid-state reaction method (SSRM) and treated at temperatures of 1300 °C, 1200 °C, and 1100 °C. The structural characteristics of the ceramics were analyzed by XRD and FT-IR. The results indicated a $CaTiO_3$ phase formation with an orthorhombic structure. The size of the crystallites was in the range of 27–36 nm and was found to increase as the temperatures increased. The relative density showed an increase from 93% to 96% as the temperatures varied from 1100 °C to 1300 °C. The impact of temperature on the radiation-protecting characteristics of the $CaTiO_3$ ceramic was assessed using the Monte Carlo simulation (MCS). There was a slight decrease in the γ-photons average track length with a raising of the temperature. At a γ-photon energy of 0.662 MeV, the γ-photons' average track lengths diminished from 3.52 cm to 3.38 cm by raising the temperature from 1100 °C to 1300 °C. The illustrated decrease in the γ-photons average track length affected the linear attenuation coefficient (μ) where the μ increased from 0.28 to 0.30 cm^{-1} with a rising temperature from 1100 °C to 1300 °C.

Keywords: $CaTiO_3$; structure; solid-state reaction; radiation shielding; Monte Carlo

Citation: Hannachi, E.; Sayyed, M.I.; Hashim, S.; Mahmoud, K.; Slimani, Y. Theoretical Examination of the Radiation Protecting Properties of $CaTiO_3$ Material Sintered at Different Temperatures. *Crystals* **2023**, *13*, 120. https://doi.org/10.3390/cryst13010120

Academic Editor: Maria Gazda

Received: 19 December 2022
Revised: 3 January 2023
Accepted: 8 January 2023
Published: 10 January 2023

1. Introduction

In recent years, the exploitation of ionizing radiation has spread in various sectors such as medicine, agriculture, infrastructure utility, military, etc. [1–3]. Ionizing radiation, including γ rays, is released by radionuclides and can spread into the environment, can easily penetrate human bodies and walls, and is difficult to be controlled. These ionizing radiations harm any living organisms and they can result in skin burns, white blood cell drops, and the annihilation and modification of cells resulting in cancer [4]. Therefore, providing highly efficient shielding shields to avoid the transmission and propagation of these radiations is essential. Traditionally, lead (Pb) is utilized as an efficient protecting material; however, due to Pb itself being dangerous [5], a robust justification is presented for searching for better alternative materials. The research direction, so far, has been engrossed with concretes [6], and glass [7–9] that can be efficient for radiation shielding applications.

Recently, however, ceramics have received significant interest owing to their potential to adjust to structures, the ease of materials accessibility, and a low cost. Other benefits are a high strength, low thermal expansion, controllable properties, non-toxic materials, and a high melting point [10]. Ceramics have been employed in diverse industrial and medical applications while additionally, they have become highly desirable materials for radiation protection purposes. For instance, Oto et al. prepared standard and doped

ceramics and determined their shielding properties against γ and neutron radiation [11]. Jawad et al. used eight types of ceramic materials and tested them against a γ-ray [12]. F. Akman et al. [13] examined the radiation-protecting characteristics of some oxide-type ceramics, and E. Hannachi et al. examined the radiation protection properties of some kinds of ceramics [14–16].

ABO_3 perovskite-based ceramics have been widely used in diverse fields such as photocatalysis, energy harvesting, multi-electronic functional apparatuses, photovoltaic cells, batteries, and electromagnetic interference shielding. These types of ceramic materials display some interesting properties such as ferroelectricity, dielectric, piezoelectricity, electro-optical, and photo-restrictive features [17,18]. These properties make them very wanted in practical areas involving metallurgy, biotechnology, materials science, electronic engineering, etc. Additionally, ABO_3 materials have been used in microwave absorption and have proven their capabilities in the radiation-protecting field [19–22].

One of the well-known ABO_3 perovskite-based ceramics is calcium titanate ($CaTiO_3$). $CaTiO_3$ was firstly discovered in mineral form by the mineralogist Gustav Rose. As a ceramic material, $CaTiO_3$ was extensively exploited in electronic apparatuses and it is the main constituent of Synroc (a kind of synthetic rock employed for nuclear waste storing) [23]. $CaTiO_3$ displays, below 1380 K, an orthorhombic structure. The crystalline structure of this ceramic material can be changed from being orthorhombic to tetragonal to cubic with an increasing temperature [24,25]. $CaTiO_{,3}$ displays a bandgap energy value of around 3.5 eV [26]. In addition, $CaTiO_3$ has been proposed as the actinide host phase in various forms of high-level radioactive waste titanate ceramics [27]. It has been reported that the properties of $CaTiO_3$ are affected by the effect of radiation [27–29].

The current study focuses on the radiation-shielding characteristics of perovskite-based ceramic materials with the parent mineral $CaTiO_3$ chosen as a case study. The effect of temperature on the structural evolution, physical and radiation-protecting peculiarities was studied and is discussed.

2. Experiment

2.1. Chemicals and Samples Fabrication

Calcium titanate ($CaTiO_3$) ceramics prepared under different temperatures were fabricated via the SSRM. Along with the specific stoichiometric ratio, the $CaCO_3$ (99.9%) and TiO_2 (99.9%) were used to synthesize the $CaTiO_3$ material. The chemicals were used as they were received. Firstly, they were mixed in an agate mortar and pestle, then, they were placed in a ball milling machine. The obtained mixture was collected, compacted into pellets, and placed in alumina crucibles to be heat-treated at various temperatures in a furnace for 3 hrs. The heat treatment was performed at the temperatures of 1300 °C, 1200 °C, and 1100 °C. The samples were coded as Ca-1100, Ca-1200, and Ca-1300 for the ceramics heat-treated at 1100 °C, 1200 °C, and 1300 °C, respectively.

2.2. Characterization

To examine the phase and crystalline structure of the ceramic samples, the XRD powder analyses (via a X-ray Bruker D8 X-ray diffractometer) were manipulated. The patterns were registered in a range of 2θ ($25° \leq 2\theta \leq 60°$). The FT-IR data were registered on a Bruker alpha II spectrophotometer (with a wavenumber range of 400–2000 cm^{-1}).

2.3. Monte Carlo Simulation

The effect of temperature on the γ-ray protection ability was evaluated using the Monte Carlo N-Particle transport code (MCNP) [30] in the photon energy 0.022–1.408 MeV. The evaluation of the γ-ray shielding capacity was performed through an input file holding all the important information about the material, detector, source and geometry. In such a configuration, the γ-photons were emitted from a source placed at the center of the geometry along the Z direction. Moreover, the density and elemental composition of the samples were inserted to the input file through the material card, while the length and

width of the samples were inserted to the cell card. The geometry adopted in the present simulation procedure is well described in previous publications [31–33]. The detector in the current work was set to be an F4 tally to evaluate the γ-photons' average track lengths and the cutoff card was set also to stop the photon emissions after a 10^6 historical. Afterward, the mean track length was utilized to evaluate the other protective parameters according to the following equations where I_o, I_t, and I_a are the total incident photons, transmitted photons, and absorbed photons inside the material, respectively:

$$\mu\left(\mathrm{cm}^{-1}\right) = \frac{\mathrm{I}}{\mathrm{x}} \ln\left(\frac{I_o}{I_t}\right) \quad (1)$$

The thickness required to absorb half of the applied γ-photons is known as the half-value thickness ($\Delta_{0.5}$, cm). It is reversely proportional to the μ value according to Equation (2):

$$\begin{aligned} \Delta_{0.5}\ (\mathrm{cm}) &= \tfrac{\ln(2)}{\mu}\ (2) \\ TF\ (\%) &= \tfrac{I_t}{I_o} \times 100\ (3) \\ RPE\ (\%) &= \tfrac{I_a}{I_o} \times 100\ (4) \end{aligned} \quad (2)$$

3. Results and Discussion

3.1. Phase Identification

XRD measurements were completed to identify the phase and to determine the mean crystallite size of the as-prepared samples, and all the diffraction peaks shown in Figure 1 revealed the orthorhombic structure of the $CaTiO_3$ perovskite (space group Pbnm). Some very small peaks corresponding to the $CaCO_3$ as indicated by * symbols, were also detected.

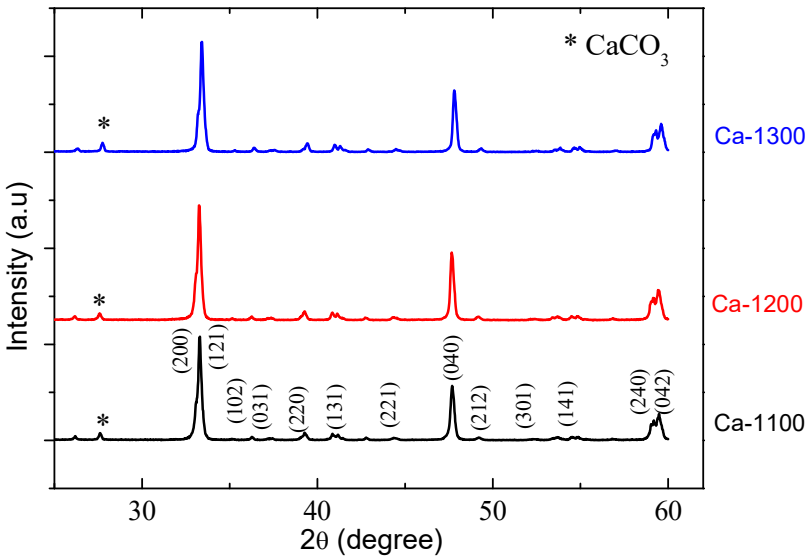

Figure 1. XRD patterns of Ca-1100, Ca-1200, and Ca-1300 ceramic samples. The asterisk refers to $CaCO_3$ phase.

The sizes of the crystallites (D) and the microstrain (ε) were computed for all the as-prepared samples using the Debye–Scherrer and Stokes and Wilson formulas, respectively, as expressed as follows [34,35]:

$$D = \frac{k\lambda}{\beta cos\theta} \quad (3)$$

$$\varepsilon = \frac{\beta}{4tan\theta} \quad (4)$$

where β is the FWHM. The dislocation density (δ) is also calculated [36]:

$$\delta = \frac{1}{D^2} \quad (5)$$

The as-prepared samples possessed D values in the range of 27–36 nm. The different parameters are tabulated in Table 1. It is clear that the D, ε, and δ changed with the temperatures. The Ca-1300 sample exhibited the highest D value. The increase in temperature stimulated a rise in the size and a decrease in the microstrain and dislocation density. This can be correlated with the formation of nuclei and aggregates formation [37]. A similar result was obtained previously by L.S. Cavalcante in $CaTiO_3$ processed in different furnaces [24]. The relative density $\rho_r = \frac{\rho_B}{\rho_{Th}}$ (where ρ_B is the bulk density and ρ_{Th} is the theoretical density which was obtained from XRD data), and the porosity percent $\left(P = \frac{\rho_{Th}-\rho_B}{\rho_{Th}} \times 100\right)$ of the as-prepared ceramics were also determined. The results are listed in Table 1. All the as-prepared ceramics displayed a ρ_r value above 90%, suggesting a good densification was reached for all the samples. It is clear also that the value of ρ_r increased from 93% to 96% as the temperature rose from 1100 °C to 1300 °C. An enhancement in the relative density was followed by a reduction in the porosity. This implies that the temperature of 1300 °C is suitable for a achieving dense ceramic with a low porosity.

Table 1. Ceramic code, crystal structure, crystallite size, relative density, and porosity percentage of as-prepared ceramics.

Ceramic Code	Temperature (°C)	Structure	D (nm)	δ 10^{15} (Lines/m^2)	Microstrain	ρ_r (%)	PP (%)
Ca-1100	1100	Orthorhombic	27.06	1.365	4.67	93	6.83
Ca-1200	1200	Orthorhombic	36.08	0.768	3.51	94	5.17
Ca-1300	1300	Orthorhombic	36.10	0.767	3.49	96	3.42

3.2. FTIR Study

The FTIR spectra of the Ca-1100, Ca-1200, and Ca-1300 ceramics are depicted in Figure 2. The strong absorption bands of ν_1 and ν_2 observed in the range of 700–400 cm^{-1} were owing to the lattice vibrations of the Ti–O and Ca–O groups [38,39]. The absorption peak at ~440 cm^{-1} matched with the Ti–O bond asymmetrical stretching vibration and the absorption peak at ~540 cm^{-1} was associated with the Ca–O bond vibrations [38,39]. The presence of the ν_1 and ν_2 bands confirm the $CaTiO_3$ phase formation for all the prepared ceramics. Another peak ν_3 was detected which might have been due to a CO_3^{2-} bending/stretching mode [40].

3.3. Radiation Shielding Study

3.3.1. Linear Attenuation Coefficient (μ)

The μ values (μ, cm^{-1}) describe the aptitude of a prepared ceramic sample to attenuate and resist the passing of energetic photons. In the current work, the μ values estimated by the Monte Carlo technique (MCNP code) in a 0.022–1.405 MeV energy range covered almost all of the γ-ray energies emitted from known radioactive sources. As is well-known and as shown in Figure 3, the μ values for the samples decreased with a rise in the energy. The mentioned decrease was caused by the effect of photoelectric interaction (PE) and Compton scattering interactions (SC) [41–43], where the interaction cross-section varied inversely with $E^{3.5}$ and E, respectively. The current results depict an exponential decrease in μ from 27.924 to 0.195 cm^{-1} (for the Ca-1100), from 28.445 to 0.199 cm^{-1} (for the Ca-1200), and from 29.113 to 0.204 cm^{-1} (for the Ca-1300), as the γ-photon energy increased from 0.022 to 1.408 MeV. Previous findings showed also that the μ values were highly affected by the sintering temperature. Figure 4 illustrates that the μ values increased with a rising sintering temperature of the fabricated ceramic samples. For example, at an energy of 0.662 MeV, the

μ values increased from 0.284 to 0.296 cm^{-1} with a rising sintering temperature from 1100 to 1300 °C, respectively. The mentioned improvement in the μ values was related to the pore size and density of the ceramic samples, where increasing the sintering temperatures caused a substantial diminution in the pores of the samples [44]. The decrease in pore size affected the compaction of, as well as the density of, the samples where the highest relative density was obtained for the Ca-1300 ceramic. Thus, the μ values increased with a rise in the sintering temperature as well.

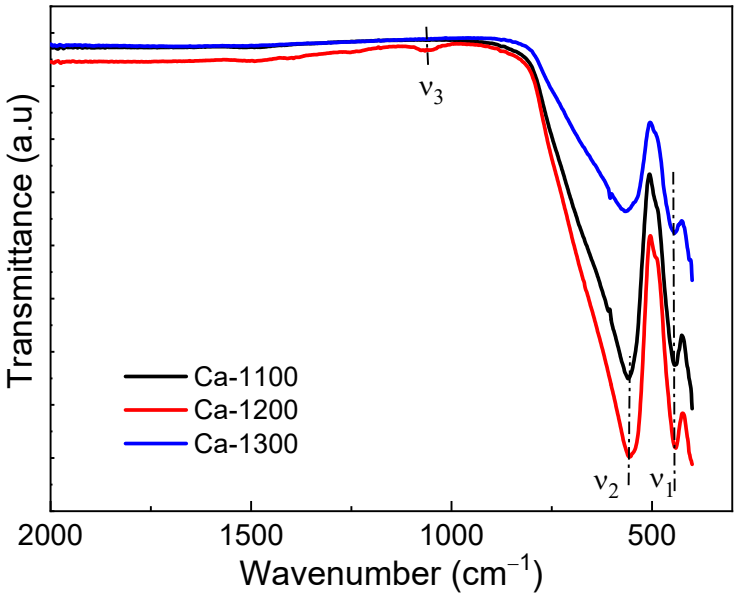

Figure 2. FTIR spectra of Ca-1100, Ca-1200, and Ca-1300 ceramic samples.

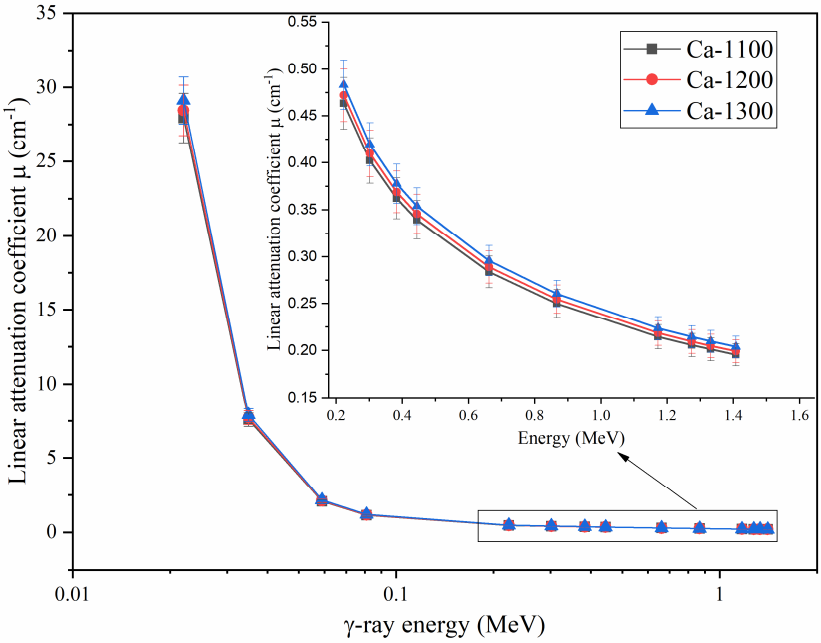

Figure 3. The μ value variations versus the incident γ-photon energies.

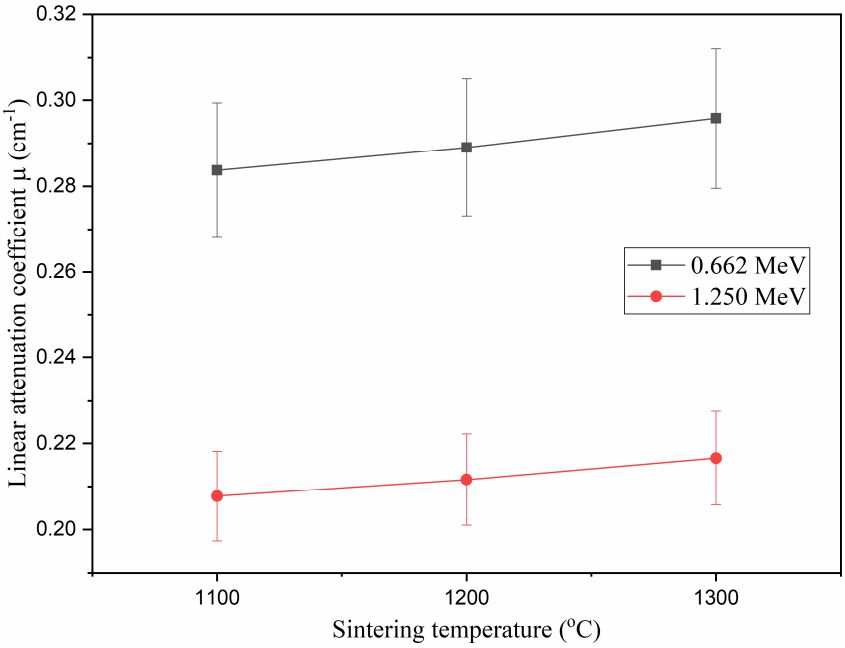

Figure 4. Dependence of the μ values on the temperature.

3.3.2. Half-Value Thickness ($\Delta_{0.5}$)

The $\Delta_{0.5}$ ($\Delta_{0.5}$, cm) is the parameter describing the thickness of the ceramic able to shield half of the incident γ-photons. In this study, the $\Delta_{0.5}$ values were affected by the energy and the sintering temperature. The obtained results show that the high γ-photon energies required a larger thickness of the synthesized ceramic samples while the lower γ-photon energies less than 0.081 MeV required several micrometers from the fabricated ceramics to shield half of the incident photons. On the other hand, the intermediate γ-photon energies between 0.1 and 1.4 MeV required $\Delta_{0.5}$ values between 1 and 3.5 cm. The increase in $\Delta_{0.5}$ values is correlated to the reverse relation between the $\Delta_{0.5}$ and the μ values, where $\Delta_{0.5} = 0.693/\mu$. The second important factor affecting the $\Delta_{0.5}$ was the sintering temperature. Figure 5 depicts that the $\Delta_{0.5}$ values at a γ-photon energy of 0.662 MeV decreased from 2.443 to 2.343 cm with raising the sintering temperature between 1100 and 1300 °C, respectively. Raising the sintering temperature decreased the pore size inside the ceramic samples which led to a raising of the sample compaction. Thus, the resistance of the samples to passing the γ-photons increased in correlation with an improvement in the μ values and a lessening in the $\Delta_{0.5}$ values.

3.3.3. Equivalent Thickness (Δ_{eq})

At a defined γ-photon energy, Δ_{eq} (Δ_{eq}, cm) describes the thickness of a prepared sample which has the similar protecting capacity as a sheet of pure Pb with a thickness of 1 cm. In the present work, the calculated values for the Δ_{eq} were found to be affected by the incident γ-photon energy and the fabrication sintering temperature. As illustrated in Figure 6, the values of Δ_{eq} reached a larger thickness at a low γ-photon energy, then, the Δ_{eq} values reduced exponentially with a rising incident γ-photon energy. For instance, the Δ_{eq} values at 0.022 MeV, were 27.40, 26.90, and 26.28 cm for the samples Ca-1100, Ca-1200, and Ca-1300, respectively. Then, the Δ_{eq} decreased exponentially with a rise in the γ-photon energy. The reduction in Δ_{eq} values was associated with the higher decrease in the values of the μ of pure Pb compared to the diminution in the μ values of the sample at the same γ-ray energy. At an energy of 1.408 MeV, the Δ_{eq} values dropped to 3.14, 3.08, and 3.01 cm for the ceramic samples of Ca-1100, Ca-1200, and Ca-1300, respectively. The sintering temperature was found also to affect the Δ_{eq} values. Figure 7 shows that the values of the Δ_{eq} reduced linearly with a rising sintering temperature. For example, the Δ_{eq} values diminished from 4.40 to 4.22 cm with a rising temperature from 1100 to 1300 °C.

As previously illustrated, the increase in the sintering temperature induced a noteworthy reduction in the porosity of the samples which increased the compactness and density of the ceramics. Thus, the fabricated ceramics samples' μ values increased in association with a decrease in the Δ_{eq} values.

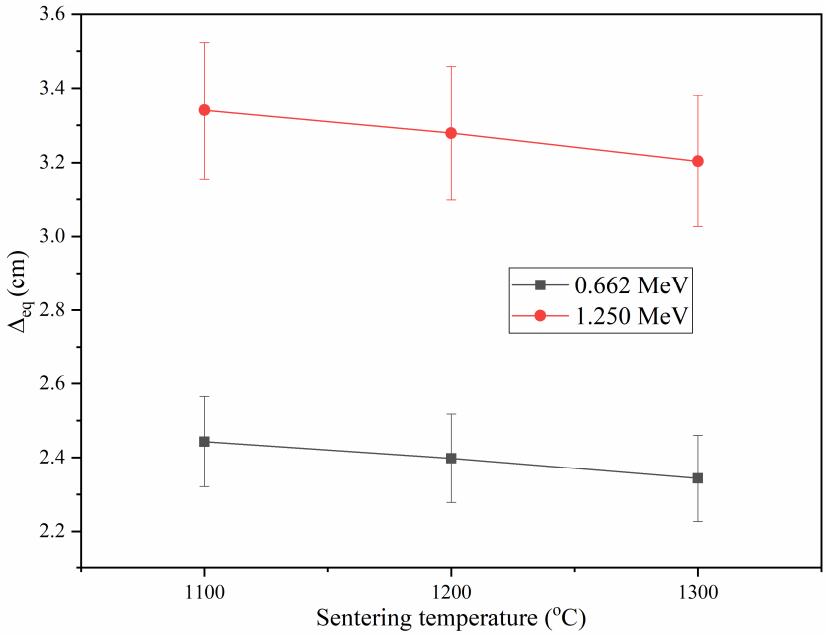

Figure 5. Effect of sintering temperature on the half value thickness $\Delta_{0.5}$ of the fabricated ceramic samples.

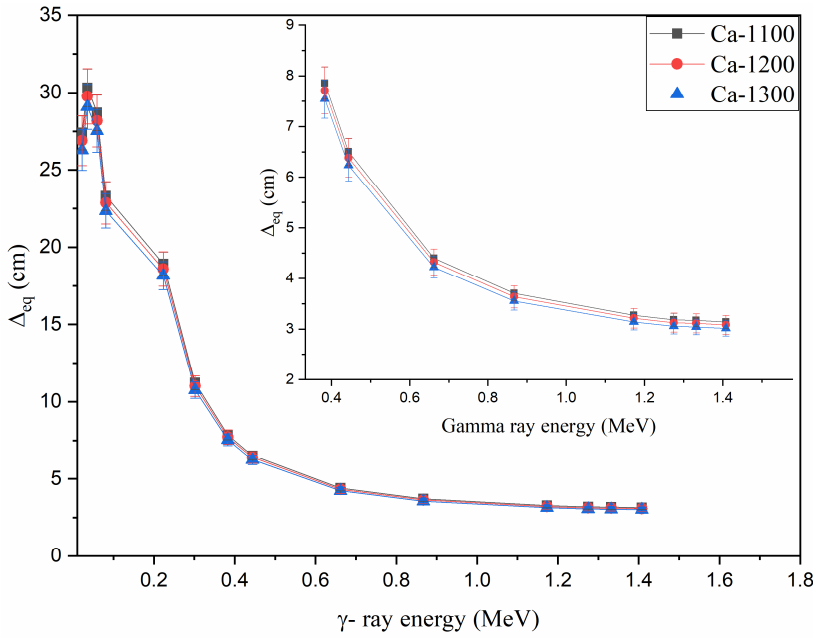

Figure 6. Dependence of the equivalent thickness on the incident γ-ray photons.

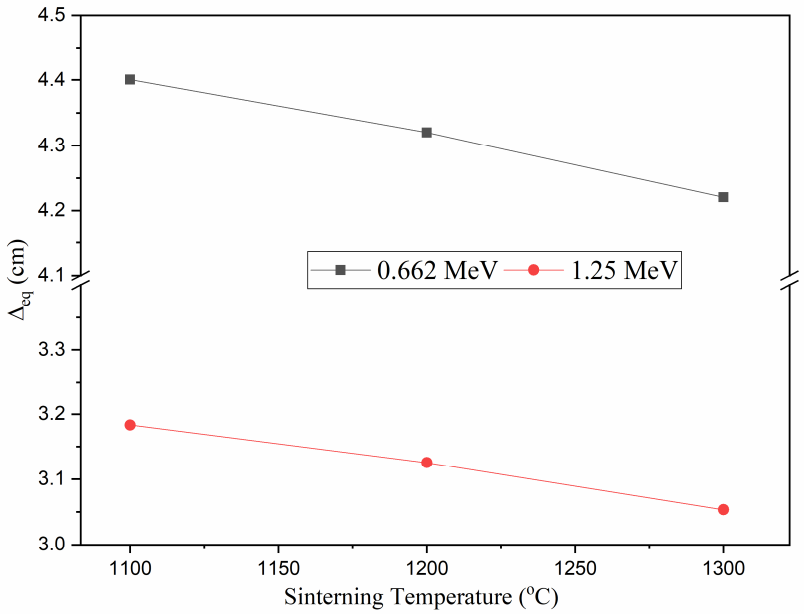

Figure 7. Variations of the (Δ_{eq}, cm) values versus the sintering temperature.

3.3.4. Radiation Protection Efficiency (RPE) and Transmission Factor (TF)

The TF (%) is a shielding factor that compares the number of photons entering protective matter to the incident photons' total number (see Equation (3)) while the RPE (%) compares the number of absorbed photons in a protecting thickness to the total number of photons (see Equation (4)). One of the current work's goals was to assess the impact of the ceramic thickness and sintering temperature on the TF and RPE. Regarding the effect of the ceramic thickness, Figure 8 illustrates that the TF decreased gradually with a growing ceramic thickness. For instance, at a fixed energy of 0.662 MeV, the TF for the ceramic sample Ca-1300 reduced by 59.5% with a growing thickness of the sample from 0.35 cm to 2 cm. Additionally, the RPE values showed a gradual increase with a rising thickness of the ceramics whereas the RPE for the Ca-1300 ceramic sample increased by 40.5% with a rising ceramic thickness from 0.25 to 2 cm. The decrease in the TF values as well as the increase in the RPE were attributed to the mean track length of the γ-photons inside the fabricated samples. Increasing the sample thickness higher than the track length of the γ-photons caused an intensification in the collisions among the photons and the atoms; therefore, the quantity of the γ energy exhausted in the material thickness was related to a diminution in the photons penetrating the stated thickness. Consequently, the RPE of the material increased followed by a decrease in the TF. Regarding the sintering temperature effect on the TF and RPE values, at a fixed energy of 0.662 MeV, Figure 9 illustrates that the TF was reduced while the RPE was enhanced with a rising sintering temperature. For example, a thickness of 1 cm slightly reduced the TF from 75.30 to 74.39%, whereas the RPE increased from 24.7 to 25.6% with a rising sintering temperature of the samples. This enhancement in the RPE with the rising sintering temperatures was attributed to the enhancement in the ceramic density when raising the sintering temperature between 1100 and 1300 °C.

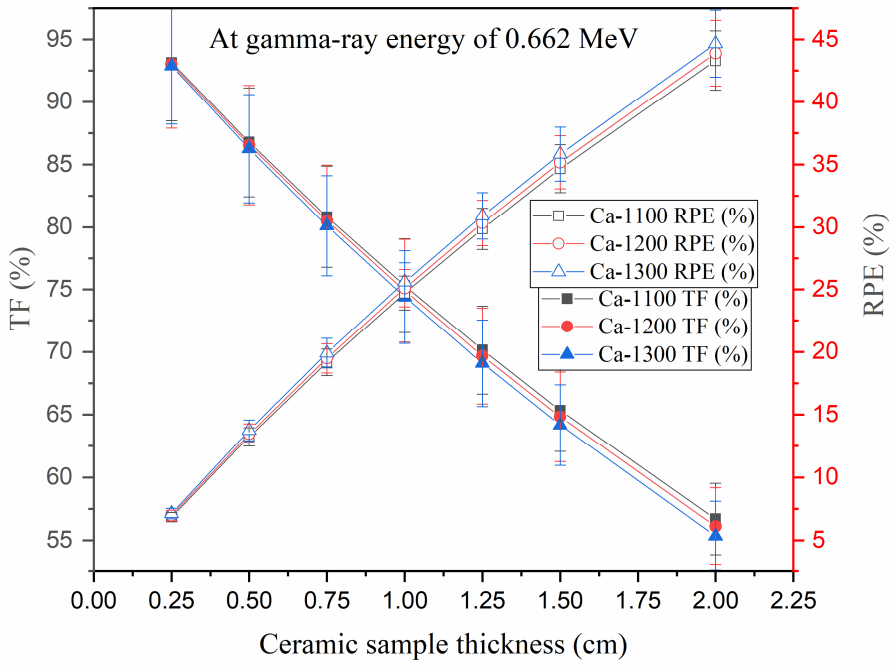

Figure 8. Variation of both TF and RPE versus the thickness of the ceramic sample.

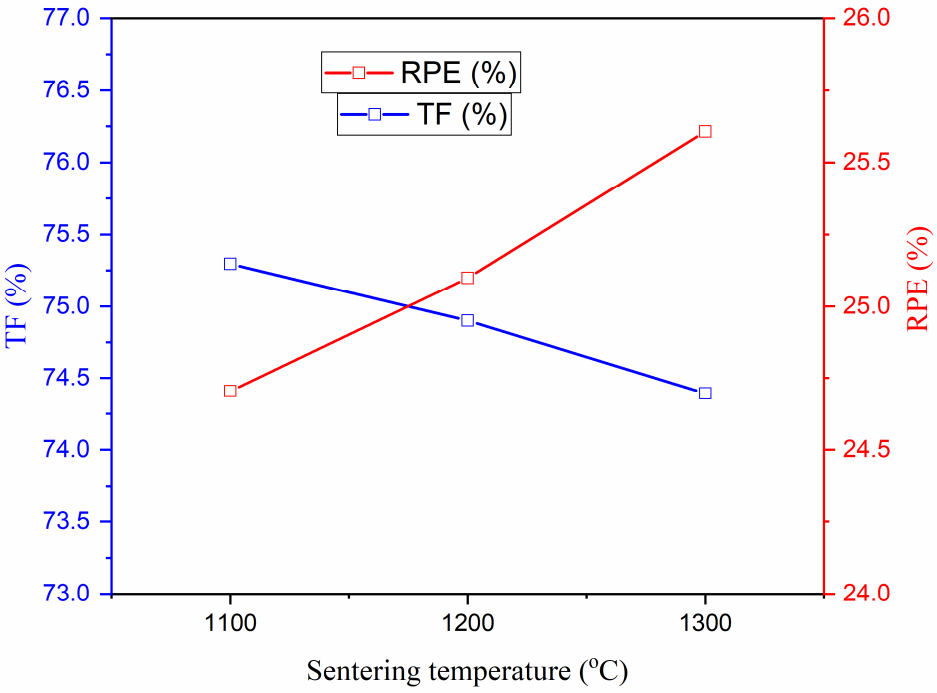

Figure 9. Variation of both TF and RPE versus the sintering temperature.

4. Conclusions

We have reported the structure and radiation-protecting features of a $CaTiO_3$ ceramic sample. Focus was applied to the effect of temperatures on the performance of the ceramic. Three samples were prepared using different temperatures. Then, the as-prepared ceramics were examined by XRD and FTIR techniques. The results showed the successful formation of a desired $CaTiO_3$ ceramic with an orthorhombic structure. The crystallite size and the relative density followed the following orders (27.06 nm < 36.08 nm < 36.10 nm) and (93% < 94% < 96%), respectively, as the temperature rose from 1100 °C to 1300 °C. The porosity was also calculated and found to be minimal for the Ca-1300 ceramic. The results

suggested that a temperature of 1300 °C led to the creation of a dense $CaTiO_3$ ceramic with a low porosity. The correlation between temperatures and the radiation-protecting peculiarities was established. The γ-ray protective properties were evaluated using the Monte Carlo simulation code in the energy ranging between 22 keV and 1408 keV. In the mentioned range of the γ-ray energy, the highest μ values were achieved for the ceramics prepared at a temperature of 1300 °C (i.e., Ca-1300). The μ values for the Ca-1300 reduced from 29.11 cm^{-1} to 0.20 cm^{-1}, by raising the energy from 22 keV to 1408 keV, respectively. Moreover, the TF values reduced from 75.30 to 74.39%, while the RPE increased from 24.7 to 25.6% with a rising sintering temperature from 1100 °C to 1300 °C, respectively.

Author Contributions: Conceptualization, E.H.; Methodology, E.H. and Y.S.; Formal analysis, E.H., M.I.S., S.H. and K.M.; Investigation, E.H., M.I.S. and K.M.; Resources, E.H. and Y.S.; Supervision, E.H. and M.I.S.; Project administration, S.H.; Funding acquisition, S.H.; Software, M.I.S. and K.M.; Validation, Y.S.; Writing—original draft, E.H., M.I.S., K.M. and Y.S., Writing—review & editing, E.H., M.I.S. and K.M. All authors have read and agreed to the published version of the manuscript.

Funding: M.I. Sayyed and S. Hashim gratefully acknowledge the Universiti Teknologi Malaysia for providing Prominent Visiting Researcher Scheme (RJ3000.7113.3F000) initiatives under the Department Deputy of Vice-Chancellor (Research and Innovation).

Institutional Review Board Statement: Not applicable.

Informed Consent Statement: Not applicable.

Data Availability Statement: Not applicable.

Acknowledgments: The authors are also thankful to the Institute for Research and Medical Consultations (IMRC) of Imam Abdulrahman Bin Faisal University (IAU–Saudi Arabia) for providing laboratory facilities. M.I. Sayyed and S. Hashim gratefully acknowledge the Universiti Teknologi Malaysia for providing Prominent Visiting Researcher Scheme (RJ3000.7113.3F000) initiatives under the Department Deputy of Vice-Chancellor (Research and Innovation).

Conflicts of Interest: The authors declare no conflict of interest.

References

1. AbuAlRoos, N.J.; Amin, N.A.B.; Zainon, R. Conventional and new lead-free radiation shielding materials for radiation protection in nuclear medicine: A review. *Radiat. Phys. Chem.* **2019**, *165*, 108439. [CrossRef]
2. Boice, J., Jr.; Dauer, L.T.; Kase, K.R.; Mettler, F.A., Jr.; Vetter, R.J. Evolution of radiation protection for medical workers. *Br. J. Radiol.* **2020**, *93*, 20200282. [CrossRef]
3. Al-Hadeethi, Y.; Sayyed, M.I. BaO–Li2O–B2O3 glass systems: Potential utilization in gamma radiation protection. *Prog. Nucl. Energy* **2020**, *129*, 103511. [CrossRef]
4. Askin, A.; Buddemeier, B.; Alai, M.; Yu, K. *Centers for Disease Control and Prevention (CDC) Radiation Hazard Scale Data Product Review Feedback Report*; No. LLNL-TR-738819; Lawrence Livermore National Lab.(LLNL): Livermore, CA, USA, 2017.
5. Ogawa, M.; Nakajima, Y.; Kubota, R.; Endo, Y. Two cases of acute lead poisoning due to occupational exposure to lead. *Clin. Toxicol.* **2008**, *46*, 332–335. [CrossRef] [PubMed]
6. Tyagi, G.; Singhal, A.; Routroy, S.; Bhunia, D.; Lahoti, M. Radiation Shielding Concrete with alternate constituents: An approach to address multiple hazards. *J. Hazard. Mater.* **2021**, *404*, 124201. [CrossRef] [PubMed]
7. Sayyed, M.I.; Dong, M.G.; Tekin, H.O.; Lakshminarayana, G.; Mahdi, M.A. Comparative investigations of gamma and neutron radiation shielding parameters for different borate and tellurite glass systems using WinXCom program and MCNPX code. *Mater. Chem. Phys.* **2018**, *215*, 183–202. [CrossRef]
8. Agar, O.; Khattari, Z.Y.; Sayyed, M.I.; Tekin, H.O.; Al-Omari, S.; Maghrabi, M.; Zaid, M.H.; Kityk, I.V. Evaluation of the shielding parameters of alkaline earth based phosphate glasses using MCNPX code. *Results Phys.* **2019**, *12*, 101–106. [CrossRef]
9. Albarzan, B.; Almuqrin, A.H.; Koubisy, M.S.; Wahab, E.A.; Mahmoud, K.A.; Shaaban, K.; Sayyed, M.I. Effect of Fe_2O_3 doping on structural, FTIR and radiation shielding characteristics of aluminium-lead-borate glasses. *Prog. Nucl. Energy* **2021**, *141*, 103931. [CrossRef]
10. Otitoju, T.A.; Okoye, P.U.; Chen, G.; Li, Y.; Okoye, M.O.; Li, S. Advanced ceramic components: Materials, fabrication, and applications. *J. Ind. Eng. Chem.* **2020**, *85*, 34–65. [CrossRef]
11. Oto, B.; Kavaz, E.; Durak, H.; Aras, A.; Madak, Z. Effect of addition of molybdenum on photon and fast neutron radiation shielding properties in ceramics. *Ceram. Int.* **2019**, *45*, 23681–23689. [CrossRef]
12. Jawad, A.A.; Demirkol, N.; Gunoğlu, K.; Akkurt, I. Radiation shielding properties of some ceramic wasted samples. *Int. J. Environ. Sci. Technol.* **2019**, *16*, 5039–5042. [CrossRef]

13. Akman, F.; Khattari, Z.Y.; Kaçal, M.R.; Sayyed, M.I.; Afaneh, F. The radiation shielding features for some silicide, boride and oxide types ceramics. *Radiat. Phys. Chem.* **2019**, *160*, 9–14. [CrossRef]
14. Hannachi, E.; Sayyed, M.I.; Slimani, Y.; Elsafi, M. Experimental study of yttrium-based ceramic systems containing nanomaterials for gamma radiation protecting applications. *App. Phys. A* **2022**, *128*, 1–9. [CrossRef]
15. Hannachi, E.; Sayyed, M.I.; Mahmoud, K.A.; Slimani, Y. Correlation between the structure, grain size distribution and radiation shielding peculiarities of YBCO ceramics prepared by two different milling methods. *Appl. Phys. A* **2022**, *128*, 1–8. [CrossRef]
16. Hannachi, E.; Sayyed, M.I.; Slimani, Y.; Elsafi, M. Experimental investigation on the physical properties and radiation shielding efficiency of YBa2Cu3Oy/M@ M3O4 (M= Co, Mn) ceramic composites. *J. Alloys Compd.* **2022**, *904*, 164056. [CrossRef]
17. Slimani, Y.; Selmi, A.; Hannachi, E.; Almessiere, M.A.; AlFalah, G.; AlOusi, L.F.; Yasin, G.; Iqbal, M. Study on the addition of SiO2 nanowires to $BaTiO_3$: Structure, morphology, electrical and dielectric properties. *J. Phys. Chem. Solids* **2021**, *156*, 110183. [CrossRef]
18. Slimani, Y.; Shirsath, S.E.; Hannachi, E.; Almessiere, M.A.; Aouna, M.M.; Aldossary, N.E.; Yasin, G.; Baykal, A.; Ozçelik, B.; Ercan, I. $(BaTiO_3)_{1-x}+(Co_{0.5}Ni_{0.5}Nb_{0.06}Fe_{1.94}O_4)_x$ nanocomposites: Structure, morphology, magnetic and dielectric properties. *J. Am. Ceram. Soc.* **2021**, *104*, 5648–5658. [CrossRef]
19. Tong, Z.; Yao, Q.; He, Q.; Deng, J.; Wang, J.; Zhou, H.; Rao, G. Effect of microcosmic regulation of unit cells bonding on microwave absorption properties of perovskite structure $GdFeO_3$. *Materialia* **2021**, *20*, 101263. [CrossRef]
20. Hannachi, E.; Sayyed, M.I.; Mahmoud, K.A.; Slimani, Y.; Akhtar, S.; Albarzan, B.; Almuqrin, A.H. Impact of tin oxide on the structural features and radiation shielding response of some ABO_3 perovskites ceramics (A= Ca, Sr, Ba; B= Ti). *Appl. Phys. A* **2021**, *127*, 1–12. [CrossRef]
21. Slimani, Y.; Hamad, M.K.; Olarinoye, I.O.; Alajerami, Y.S.; Sayyed, M.I.; Almessiere, M.A.; Mhareb, M.H. Mhareb. Determination of structural features of different Perovskite ceramics and investigation of ionizing radiation shielding properties. *J. Mater. Sci. Mater. Electron.* **2021**, *32*, 20867–20881. [CrossRef]
22. Hannachi, E.; Mahmoud, K.A.; Sayyed, M.I.; Slimani, Y. Slimani. Structure, optical properties, and ionizing radiation shielding performance using Monte Carlo simulation for lead-free BTO perovskite ceramics doped with ZnO, SiO_2, and WO_3 oxides. *Mater. Sci. Semicond. Process.* **2022**, *145*, 106629. [CrossRef]
23. Ringwood, A.E.; Kesson, S.E.; Reeve, K.D.; Levins, D.M.; Ramm, E.J. *Radioactive Waste Forms for the Future*; Lutze, W., Ewing, R.C., Eds.; IAEA: Vienna, Austria, 1988; pp. 233–334.
24. Cavalcante, L.S.; Marques, V.S.; Sczancoski, J.C.; Escote, M.T.; Joya, M.R.; Varela, J.A.; Santos, M.R.; Pizani, P.S.; Longo, E. Synthesis, structural refinement and optical behavior of $CaTiO_3$ powders: A comparative study of processing in different furnaces. *Chem. Eng. J.* **2008**, *143*, 299–307. [CrossRef]
25. Eglitis, R.I.; Popov, A.I. Systematic trends in (0 0 1) surface ab initio calculations of ABO_3 perovskites. *J. Saudi Chem. Soc.* **2018**, *22*, 459–468. [CrossRef]
26. Ueda, K.; Yanagi, H.; Noshiro, R.; Hosono, H.; Kawazoe, H. Vacuum ultraviolet reflectance and electron energy loss spectra of. *J. Phys. Condens. Matter* **1998**, *10*, 3669. [CrossRef]
27. Smith, K.L.; Zaluzec, N.J. The displacement energies of cations in perovskite ($CaTiO_3$). *J. Nucl. Mater.* **2005**, *336*, 261–266. [CrossRef]
28. Weber, W.J.; Ewing, R.C. Radiation effects in crystalline oxide host phases for the immobilization of actinides. *MRS Online Proc. Libr. (OPL)* **2002**, *713*, JJ3.1.1–JJ3.1.12. [CrossRef]
29. Zhang, Z.; Blackford, M.G.; Lumpkin, G.R.; Smith, K.L.; Vance, E.R. Aqueous dissolution of perovskite (CaTiO3): Effects of surface damage and [Ca2+] in the leachant. *J. Mater. Res.* **2005**, *20*, 2462–2473. [CrossRef]
30. X-5 Monte Carlo Team. *MCNP—A General Monte Carlo N-Particle Transport Code*; Version 5, La-Ur-03-1987. II; Los Alamos National Laboratory: Los Alamos, Mexico, 2003.
31. Al-Harbi, N.; Sayyed, M.I.; Al-Hadeethi, Y.; Kumar, A.; Elsafi, M.; Mahmoud, K.A.; Khandaker, M.U.; Bradley, D.A. A novel $CaO–K_2O–Na_2O–P_2O_5$ glass systems for radiation shielding applications. *Radiat. Phys. Chem.* **2021**, *188*, 109645. [CrossRef]
32. Sayyed, M.I.; Zaid, M.H.; Effendy, N.; Matori, K.A.; Lacomme, E.; Mahmoud, K.A.; AlShammari, M.M. The influence of PbO and Bi_2O_3 on the radiation shielding and elastic features for different glasses. *J. Mater. Res. Technol.* **2020**, *9*, 8429–84381. [CrossRef]
33. Naseer, K.A.; Marimuthu, K.; Mahmoud, K.A.; Sayyed, M.I. The concentration impact of Yb3+ on the bismuth boro-phosphate glasses: Physical, structural, optical, elastic, and radiation-shielding properties. *Radiat. Phys. Chem.* **2021**, *188*, 109617. [CrossRef]
34. Hannachi, E.; Mahmoud, K.A.; Sayyed, M.I.; Slimani, Y. Effect of sintering conditions on the radiation shielding characteristics of YBCO superconducting ceramics. *J. Phys. Chem. Solids* **2022**, *164*, 110627. [CrossRef]
35. Ortiz, A.L.; Shaw, L. X-ray diffraction analysis of a severely plastically deformed aluminum alloy. *Acta Mater.* **2004**, *52*, 2185–2197. [CrossRef]
36. Singh, P.; Yadav, R.S.; Rai, S.B. Enhanced photoluminescence in a Eu3+ doped CaTiO3 perovskite phosphor via incorporation of alkali ions for white LEDs. *J. Phys. Chem. Solids* **2021**, *151*, 109916. [CrossRef]
37. Zhou, G.; Lü, M.; Gu, F.; Xu, D.; Yuan, D. Morphology-controlled synthesis, characterization and growth mechanism of PbWO4 nano and macrocrystals. *J. Cryst. Growth* **2005**, *276*, 577–582. [CrossRef]
38. Lozano-Sánchez, L.M.; Lee, S.W.; Sekino, T.; Rodríguez-González, V. Practical microwave-induced hydrothermal synthesis of rectangular prism-like CaTiO 3. *CrystEngComm* **2013**, *15*, 2359–2362. [CrossRef]

39. Peng, C.; Hou, Z.; Zhang, C.; Li, G.; Lian, H.; Cheng, Z.; Lin, J. Synthesis and luminescent properties of $CaTiO_3$: Pr^{3+} microfibers prepared by electrospinning method. *Opt. Express* **2010**, *18*, 7543–7553. [CrossRef] [PubMed]
40. Lopes, C.D.; Limirio, P.H.; Novais, V.R.; Dechichi, P. Fourier transform infrared spectroscopy (FTIR) application chemical characterization of enamel, dentin and bone. *Appl. Spectrosc. Rev.* **2018**, *53*, 747–769. [CrossRef]
41. Abouhaswa, A.S.; Sayyed, M.I.; Mahmoud, K.A.; Al-Hadeethi, Y. Direct influence of mercury oxide on structural, optical and shielding properties of a new borate glass system. *Ceram. Int.* **2020**, *46*, 17978–17986. [CrossRef]
42. El-Agawany, F.I.; Mahmoud, K.A.; Akyildirim, H.; Yousef, E.S.; Tekin, H.O.; Rammah, Y.S. Rammah, Physical, neutron, and gamma-rays shielding parameters for Na_2O-SiO_2-PbO glasses. *Emerg. Mater. Res.* **2021**, *10*, 1–9.
43. Abouhaswa, A.S.; Sayyed, M.I.; Altowyan, A.S.; Al-Hadeethi, Y.; Mahmoud, K.A. Synthesis, structural, optical and radiation shielding features of tungsten trioxides doped borate glasses using Monte Carlo simulation and phy-X program. *J. Non-Cryst. Solids* **2020**, *543*, 120134. [CrossRef]
44. Mouiya, M.; Bouazizi, A.; Abourriche, A.; El Khessaimi, Y.; Benhammou, A.; Taha, Y.; Oumam, M.; Abouliatim, Y.; Smith, A.; Hannache, H. Effect of sintering temperature on the microstructure and mechanical behavior of porous ceramics made from clay and banana peel powder. *Results Mater.* **2019**, *4*, 100028. [CrossRef]